Chapter 9

Patterned 3D Nanostructure Arrays from Charged Aerosols

Jicheng Feng, Kiwoong Lee, and Mansoo Choi
Global Frontier Center for Multiscale Energy Systems,
Seoul National University, Seoul 08826, Republic of Korea
Department of Mechanical and Aerospace Engineering
Seoul National University, Seoul 08826, Republic of Korea
mchoi@snu.ac.kr

Three-dimensional (3D) nano-/microstructures open up new possibilities for developing nanodevices used in sensors, electronics/optoelectronics, and energy conversion systems. In this chapter, we review a nanoscale patterning technology, coined as "electric-field-assisted aerosol lithography" (EAAL), for making arrays of complex 3D nano-/microstructures under atmospheric conditions. In EAAL, electrical charging of prepatterns leads to focusing nanoscopic electrostatic lenses that steer the deposition of charged aerosols into precisely addressable locations on a surface. The construction of 3D micro-/nanostructures requires a consistent supply of building blocks in the form of charged aerosol particles of a few nanometers in size. Spark ablation is picked to create such building blocks, and associated modifications are also introduced here.

Spark Ablation: Building Blocks for Nanotechnology
Edited by Andreas Schmidt-Ott

ISBN 978-981-4800-82-2 (Hardcover), 978-0-367-81709-1 (eBook)
www.jennystanford.com

9.1 Introduction

Well-ordered multidimensional multiscale nano-/microstructures provide a platform for creating novel nanodevices, including sensors, electronic/magnetic, and photonic devices (e.g., solar cells). Although various techniques for the fabrication of 3D micro-/nanostructures have been developed, particularly in the past decade, each existing method has its own limitation that currently hinders mass production of 3D micro-/nanostructures. For example, well-established nanofabrication techniques utilizing electron beams ([1–3]), focused ion beams [4], and laser beams [5, 6] are inherently a serial approach that requires a high-vacuum environment. Therefore, these approaches have been largely confined to laboratory scale, not available to scale up to mass production. Microcontact printing [7] that utilizes nanopatterned stamps is a parallel approach; however, apparently it has difficulty in fabricating 3D structures. The capillary force could be utilized effectively to introduce nanoparticles (NPs) into the prepatterned trench area to make well-ordered NP arrays [8, 9]. Still, the method does not favor the fabrication of 3D structures. Although 3D printing technology has been extensively explored over the past years [10–13], its resolution does not yet reach to the nanoscale. These observations suggest a strong need to develop a new way of constructing 3D nano-/microstructures in a practical manner. The preferred approach should work under atmospheric conditions and be operated in a parallel process (vs. serial direct-write or serial wire-bonding methods) to produce 3D nanostructures on a large surface area with nanometer resolution.

In this chapter, we review a new approach utilizing aerosol technology to develop 3D nano-/microstructure arrays in a practical way. The method utilizes charged aerosols that are precisely positioned into the desired location on a substrate using a process called “ion-assisted aerosol lithography” (IAAL) or “electric-field-assisted aerosol lithography” (EAAL). Throughout this chapter, we stick to the term “EAAL.” Making nanoscale-resolution 3D structures requires smaller NP building blocks down to a size of sub-10 nm. It is also important to provide unagglomerated particles to assure compact 3D structures. To achieve that, we will present a number of recent developments in spark discharge. The parallel patterning process can make complex 3D nanostructures on a surface from

microscale to macroscale and simply works under atmospheric conditions. The 3D assembly module via this method will be explained and various applications of the resultant 3D nanostructures will be introduced.

9.2 Spark Discharge Techniques for Generating a Few Nanometer-Size Unagglomerated Charged Aerosols

Spark discharge was introduced to make aerosol NPs by Schwyn et al. [14]. It consists of a pair of electrodes connected to a resistance-inductance-capacitance (RLC) circuit, as shown in Fig. 9.1. The electrodes face each other and are separated by a gap (ca. 1 mm), within which an inert gas flushes through. A constant current source continuously charges the capacitance until reaching a breakdown voltage and forms a spark discharge in the interelectrode gap. After discharging, the capacitance is recharged for preparing a consecutive spark. The process repeats itself, while the variation of the breakdown voltage appears problematic [15]. Spark energy, which is an important parameter to determine the particle properties, is proportional to the square of the breakdown voltage. The voltage variation therefore leads to non-uniformity of the generated aerosols. To keep a constant spark energy, Pfeiffer et al. and Feng et al. developed a switching RLC circuit (cf. Fig. 9.1) [16–18], which always applies the same voltage to ignite sparks. Despite the various developments, this section mainly focuses on the generation of desired NP building blocks in order to make patterned 3D nanostructures.

To make patterned 3D nanostructures with high controllability/reproducibility/scalability/resolution, we first modify size distributions of NPs generated by the spark ablation. Besides size dependence on operating parameters [18–20], electrode configurations were found important to control the particle size. Then, we increase the portion of positively charged particles to encourage the 3D nanostructure growth, since they are attracted to a negatively biased substrate and subsequently deposited there, or both polarities can be reversed accordingly. Although the NP structures were shown to reach nanoscale resolution, parallel

patterning on a large surface area of macroscale remains a challenge. To overcome that, we will also detail the development for sparking multiple pairs of electrodes in parallel. Finally, we will show how to maintain the crystallinity and purity of NPs, which make the final 3D nanostructures also preserve good crystallinity and purity, as required for certain applications.

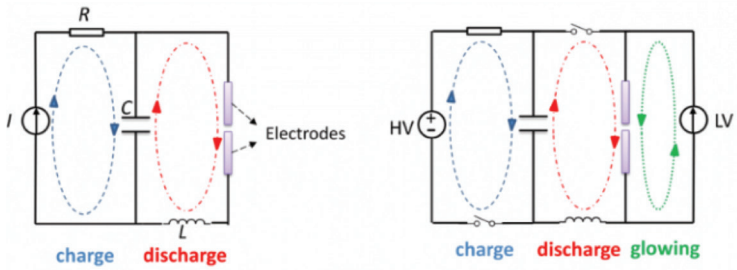

Figure 9.1 Electrical circuit for creating spark discharges. Left: Classical RLC spark circuit. Right: Switching circuit that can reach a spark repetition frequency as high as 25 kHz [16]. The switching circuit contains a continuous current source that sustains a low glowing discharge to facilitate spark ignition, too low in power to ablate the electrodes. From Ref. [17], reproduced by permission of The Royal Society of Chemistry.

9.2.1 Pin-to-Plate and Wire-in-Hole Configuration Spark Discharge

In the classical setup of spark ablation, electrode configuration is mainly based on rod-to-rod (cf. Fig. 9.2a) [21]. We found out that changing this configuration to pin-to-plate (cf. Fig. 9.2b) enables the production of unagglomerated NPs with a narrower size distribution. We attribute this to the reduction of the particle duration in the aerosol form (i.e., residence time or coagulation volume) and quickly capture them onto a substrate. Although this pin-to-plate-type spark discharge was successful in generating a few nanometer unagglomerated particles, we identified a problem of consistent production. In the case of long-term sparking, the sharp pin was significantly ablated to result in a broader size distribution than that obtained initially. Motivated by this, we developed a wire-in-hole-type electrode configuration (Fig. 9.2c). The wire-in-hole

configuration ensures a longer and more stable spark operation, because a large surface area of the wire cylinder experiences the spark strikes. As a result, this greatly improves the consistency of particle size distribution with time. Making smaller unagglomerated NPs through this way is in line with the findings from Feng et al. [19, 20], who shortened particle duration in aerosol by increasing the gas flow rate. In contrast to that, this way to make sub-10-nm particles is beneficial for printing 3D nanostructures (detailed reasons are shown later) [21, 22].

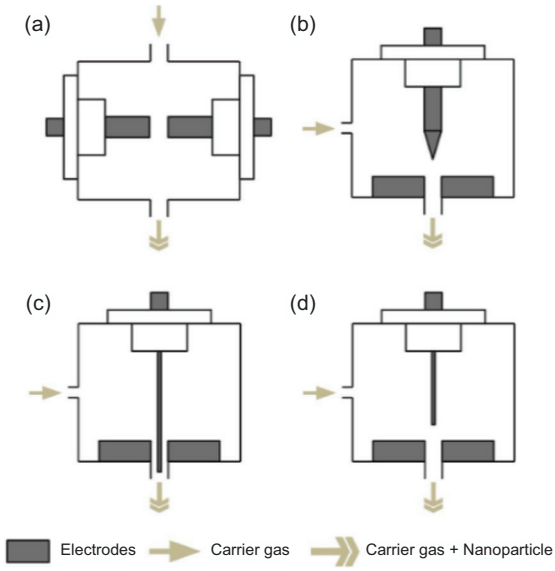

Figure 9.2 Electrode configurations in a spark chamber. (a) Rod-to-rod, (b) pin-to-plate, (c) wire-in-hole, and (d) wire-to-plate. From Ref. [21], reprinted by permission of the publisher (Taylor & Francis Ltd, http://www.tandfonline.com).

9.2.2 Enhancing NP Throughput

Given a spark energy, the NP mass production rate is proportional to the spark repetition frequency [17]. In the classical RLC circuit for initiating sparks, increasing frequency leads to premature spark discharges associated with the residual spark plasma. To minimize these premature discharges, wire-to-plate electrodes were used for a fast removal of the residual plasma. As compared to other

types of electrode configuration, such an arrangement results in an increase of not only local velocity of the carrier gas but also electrical field intensity around the spark domain [23]. On the other hand, raising the spark repetition frequency in the classical RLC circuit can develop continuous arc discharges, signaling that an upper operating frequency threshold exists in the system. Exceeding the threshold, linearity does not hold between the NP mass production rate and the frequency [17]. Much larger particles (hundreds of nanometers to a few microns) are produced in arc discharges (hot plasma temperature), thereby giving a higher mass production rate of these undesirably large particles. In the recent works of Feng et al. [17] and Pfeiffer et al. [16], they decoupled the charge and discharge cycle in a switching RLC circuit. Using that circuit, the highest possible spark frequency can reach 25 kHz. As a result, the mass production rate is enhanced by about 2 orders of magnitude, while maintaining the production of sub-10-nm particles and the virtually unlimited mixing possibilities [17].

Besides increasing NP throughput in a single electrode pair [23], we developed multiple pins to holes on a plate electrode for making parallel sparks in a chamber. Doing so, we also gained the benefit of patterning uniform NP structures on an extended surface area of 50 mm × 50 mm [24]. The uniformity of patterned 3D nanostructures was improved by a factor of 3 compared to the single-pin system (i.e., a point particle source). In the single-pin setup, the concentration of charged aerosols is inhomogeneously distributed above a large substrate, leading to taller (shorter) nanostructures at the center (edge) of the substrate [24]. When using multiple pins, the charged aerosol cloud was enlarged to well cover the entire substrate. In addition, proximity collection (i.e., the substrate was placed inside the spark chamber instead of using an extended tubing system) was applied for assembling very tiny NPs/clusters formed at the initial stage [19, 20], reflected by denser nanostructures. Similar results were obtained by increasing the flow rate. In addition, proximity collection largely preserves the charged species (e.g., charged aerosols and ions), the combination of which is essential to obtain a good focusing effect. This work therefore brings our technology into a practical use for the resulting 3D nanostructures on a macroscale.

9.2.3 Increasing the Portion of the Positively Charged Particles

Spark ablation generally produces a higher fraction of charged particles (mainly carrying one elementary charge) without the need of any charging device [25]. This fulfills the requirements of EAAL [26], which relies on a localized electric field to precisely direct charged NPs for the construction of 3D nanostructures. Evidently, increasing the portion of charged particles is the sole approach to promoting the growth of 3D nanostructures. In spark ablation, particle charging mainly stems from ion attachment [27]. To enhance the particle–ion collisions, positive ions were continuously added into the aerosols by directly connecting a second voltage source that allowed a corona discharge mode before breakdown. The amount of positively charged particles was increased by a factor of ca. 2, while those of negatively charged ones diminished by about half.

9.2.4 Generation of Highly Crystalline Silicon NPs

Spark ablation does not employ any liquid precursors/stabilizers, thereby bringing a highly pure NP surface. Considering also the high reactivity of NPs with the trace amount of reagents (e.g., O_2, probably during the production or sample transport), the NPs collected are normally covered with an oxide layer (the thickness depends on the handling process). Apart from that, oxidation of NPs induces the formation of partial amorphous structures [28, 29], which are undesirable to some applications (e.g., solar cells, quantum dots). To address this problem, hydrogen was added to the carrier gas for passivating the surface of NPs via binding hydrogen atoms there [28, 29]. As an example, the good crystallinity of produced Si NPs was confirmed by transmission electron microscopy (TEM), X-ray diffraction (XRD), and Raman spectra, whereas Fourier-transform infrared spectroscopy (FTIR) measurements showed a reduction of NP oxidation. The work provides a general approach to handling "clean" NP building blocks for 3D nanostructure arrays and toward other applications strictly requiring a highly pure NP surface.

9.3 Formation of 3D Nanostructure Arrays

3D nanostructure arrays can be made by delivering NP building blocks into precisely addressable locations predetermined on a substrate. This means that some kind of force must drive the particles to the location, and different forces were already exemplified in Section 9.1. In this chapter, we combine the Columbic force–dominated 3D assembly of charged aerosol NPs with topographically patterned substrates formed by conventional lithography. In this process, the reshaped electric field streamlines steer the transport of charged aerosols to precisely addressable locations. A prolonged deposition piles up charged NPs to form 3D nanostructures where charge dissipation can occur. This way of making 3D structure arrays remarkably reaches nanoscale resolution and operates under atmospheric conditions.

9.3.1 Electric-Field-Assisted Aerosol Lithography

Choi's group introduced the use of EAAL for patterning 3D nanostructure arrays on a surface [26]. In the method, charged aerosols together with ions of the same polarity are injected into a chamber where an electric field is applied. In the chamber, a negative voltage is applied to a substrate prepatterned by a dielectric layer (e.g., photoresist [PR]). Considering the mobility difference between ions and charged aerosols, the former move faster to accumulate on the surface of the dielectric prepatterns. Other ions are deposited onto openings of the substrate and are neutralized immediately. The ions on the surface of the prepatterns distort the originally almost flat equipotential plane into a convex-shaped equipotential plane that acts as a nanoscopic electrostatic lens around each prepattern. Later-arriving charged aerosols follow the localized electric field line near the substrate and are deposited into the openings (cf. Fig. 9.3). The degree of focusing can be manipulated by the amount of ions injected. In 2006, this method was, for the first time, explained in detail and used for parallel patterning of charged aerosol NPs of various metals [26]. It was found that the width of deposited NP pillars was about 1/6 of the width of opening patterns. As already mentioned, this focused deposition is attributed to the electrostatic

lens effect induced by either predeposited ions or a potential on the prepattern surface.

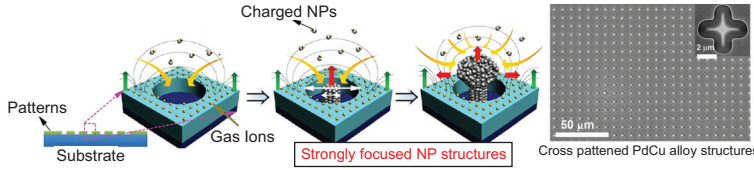

Figure 9.3 Schematic of the assembly progress of charged aerosols via EAAL. The red, green, and yellow arrows represent the growing direction of nanostructures, repelling electric forces, and direction of coming aerosols, respectively. Adapted and reprinted from Ref. [30]. © IOP Publishing. Reproduced with permission. All rights reserved.

From a theoretical perspective, the NP deposition process in EAAL can be described by a Lagrangian particle trajectory [31]. Provided that the Poisson equation was used to obtain the electric field, the particle trajectory can be calculated through the Langevin equation:

$$m_{\mathrm{p}} \frac{dv_{\mathrm{p}}}{dt} = F_{\mathrm{D}} + F_{\mathrm{B}} + F_{\mathrm{C}} + F_{\mathrm{vdW}} \tag{9.1}$$

It contains these terms: the fluid drag force F_{D} , the Brownian force F_{B}, the Coulomb force F_{C}, and the van der Waals force F_{vdW} [32–35], where m_{p}, t, and v_{p} refer to the mass of a particle, the time, and the particle velocity, respectively.

To clarify the generality of EAAL, next we discuss particle material, the number of particle charges, and the type of substrate hosting the 3D nanostructures. The particle material, in principle, can be any, depending on which aerosol technology is used for making the charged aerosol NPs. It was found that EAAL favors singly charged NPs in terms of making uniform/compact 3D nanostructures and ensuring a clean dielectric surface [36]. With respect to the substrate, conductivity is important to frame localized "funnel like" electrical field streamlines and to prevent charge accumulation during deposition. Notably, we also showed the possibility of making 3D nanostructures on a nonconductive substrate [33].

To broaden the scope of particle materials, Choi's group also used EAAL to successfully pattern protein and polystyrene NP structures [36, 37]. By electrospraying protein molecules to form charged

aerosols, the patterned micro-/nanoarrays had 50–130 nm features, even deposited into the valleys within the deep microchannels [37] In addition to polystyrene NP patterns, polymeric particle patterns were made from electrospray deposition through a mask placed on a substrate [38]. Differently, the focusing effect was produced by setting a potential difference to a conductive mask and a dielectric substrate (opposite to our case of using a dielectric mask and a conductive substrate).

Using electrospraying for producing charged aerosols, the ill-defined number of charges on particles was proven to exacerbate the focusing effect during deposition [36]. The reason for this is that more charges on a single particle [39] make it not fully follow the electric field lines due to the effect of inertia (cf. Fig. 9.4). Similar to impaction, these NPs (gaining a higher velocity than those with one elementary charge) easily deviate from the electric field lines, thus depositing onto the mask surface or the mask openings randomly. With the help of a neutralizer, the focused deposition was eventually recaptured but with inevitable particle agglomeration and a significant loss of charged particles. It is worthwhile to note that spark ablation produces a higher percentage of charged NPs, which only take one elementary charge without the need of any secondary charging device [40]. This turns out to be a key advantage for highly focused NP deposition, closely correlated to uniform/compact 3D nanostructures and a clean dielectric surface.

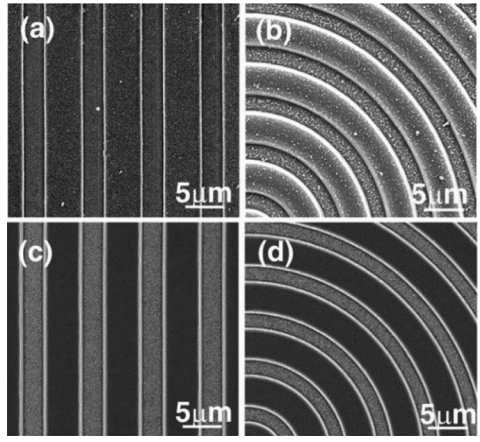

Figure 9.4 Patterned deposition for ill-defined (a, b) and well-defined (c, d) number of charges of polystyrene NPs produced by electrospraying. Reprinted from Ref. [36], with the permission of AIP Publishing.

9.3.2 3D Assembly of NPs via EAAL

A conductive substrate (e.g., a highly doped silicon wafer) is covered by a layer of dielectric materials having prepatterned open spacings. Figure 9.3a schematically shows a single-hole PR pattern (color-coded mint) covering a Si substrate (brilliant blue). Upon applying a voltage to the substrate, the charged aerosols are guided along the electric field line and subsequently deposited on the exposed conductive region in a converging manner (cf. Fig. 9.3b). Furthermore, Fig. 9.3c shows that the NP deposition develops to 3D nanostructures arrays (more details will be discussed later), followed by removal of the dielectric layer (dipping in acetone or O_2 plasma etching). Figure 9.5 provides a direct visual of cross PR patterns on a Si wafer.

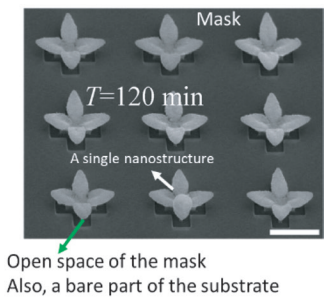

Figure 9.5 SEM image of the prepatterned substrate (with a cross pattern, made of PR; scale bar = 1.5 μm). Reprinted with permission from Ref. [41]. Copyright (2011) American Chemical Society.

As the nanostructures grow taller than the dielectric layer, their growth splits into lateral and vertical directions because of the strong repelling electric field from the PR surface (cf. Fig. 9.3c). To give a direct visual, we provide scanning electron microscopy (SEM) images (cf. Fig. 9.6) of arrays of 3D nanostructures consisting of Cu NPs on the PR prepatterned Si substrate [41, 42]. Figures 9.6a and 9.6b show the resulting 3D nanostructures when using square arrays of 1.5 μm long cross PR patterns for 90 and 120 min deposition, respectively. In this case, 3D nanostructures give fourfold flower-like shapes. Changing to square prepatterned substrates, Figs. 9.6c and 9.6d represent the resulting 3D nanostructures for NP deposition of

40 and 90 min, respectively. Therefore, it can be observed that PR patterns play an essential role in determining the shapes of the final 3D nanostructures.

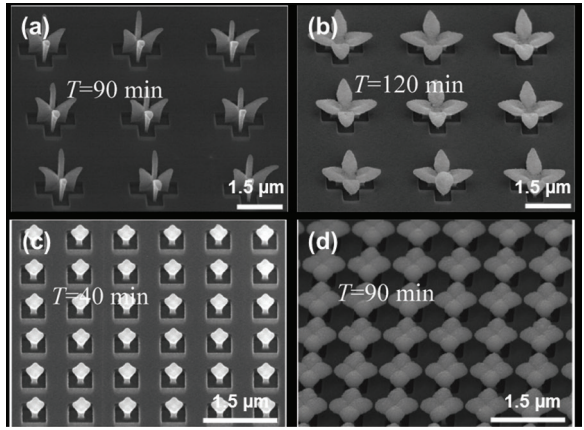

Figure 9.6 (a, b) SEM images of 3D nanostructures on PR cross patterns for 90 and 120 min deposition and (c, d) on PR square patterns for 40 and 90 min deposition. Reprinted with permission from Ref. [41]. Copyright (2011) American Chemical Society.

The final 3D nanostructures, however, can be completely different from the opening patterns (cf. Fig. 9.6). For example, a round opening can make a mushroom-like nanostructure, while a square and a cross pattern allow to make clovers and lotus petals [41]. The shape of 3D nanostructures depends on several factors, such as the arrangement of adjacent hole patterns, NP size, deposition time, surface charge density on the dielectric surface, and flow rate of charged aerosols. As shown in Fig. 9.6b,d, 3D nanostructures grow toward their neighborhoods and eventually connect to each other, regardless of the shape of the prepatterns. Such a multifurcating mechanism has been recently elaborated [34]. When nanostructures grow upward and become higher than the PR layer (cf. Fig. 9.7a), they start leaning toward the nearest structure. This is because the potential field acts like an electrical trap. At different heights from the surface of the substrate (e.g., Z = 1.5 and 2 μm relatively far from the pattern with a thickness of ca. 0.3 μm; cf. Fig. 9.7b), the potential fields are interconnected, explaining the formation of bridges among the nanostructures. In the case that the adjacent nanostructures

are sufficiently distant, one can see in Fig. 9.7c that the shape of PR patterns does determine the shape of the resulting nanostructures.

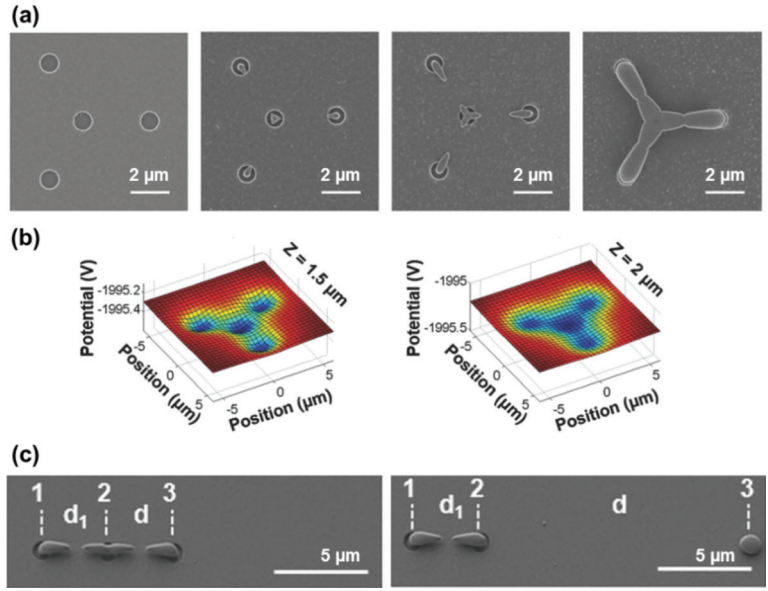

Figure 9.7 (a) SEM images of Cu nanostructures on 1 μm hole patterns at different deposition times (0, 5, 15, and 25 min). (b) Electric potential calculated at different heights of Z = 1.5 and 2 μm. (c) SEM images of three Cu nanostructures at different hole locations. d_1 = 3.5 μm, d = 3.5, and d = 14 μm. Reprinted with permission from Ref. [34]. Copyright (2016) Wiley-VCH.

To this end, we describe that EAAL can make a matrix of complex 3D structures with a single layer. The following part explores the possibility of stacking multilayers of 3D nanostructures, even feasible with different materials and dimensions. Using a prepatterned substrate may limit a vertical growth of consecutive 3D nanostructures. The height of the 3D nanostructures is more or less in the order of 1 μm. To stack a second layer vertically, we managed to deposit the NPs on top of the existing 3D nanostructures from the first deposition (cf. Fig. 9.8) [35]. Both depositions occurred within identical cross-opening prepatterns and an identical relative thickness of the PR layer. In other words, the first deposition used a PR layer with a thickness of 100 nm, while the second layer deposition had a distance of 100 nm between the top surface of the PR layer and the head of the 3D nanostructures.

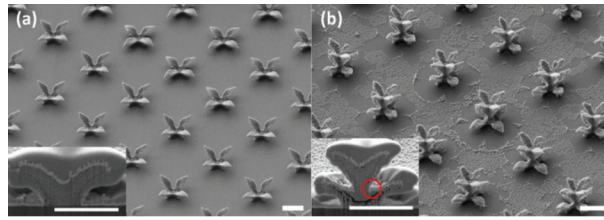

Figure 9.8 SEM images of monolayer and double-layer 3D nanostructures (scale bar = 1 μm). Reprinted from Ref. [35]. © IOP Publishing. Reproduced with permission. All rights reserved.

9.3.3 NP Focusing Mask

In 2010, Choi's group extended EAAL by eliminating the step of PR prepatterning via a so-called focusing mask concept [33]. The method employed a nonconducting stencil mask having openings, which adheres to the same principle of ion-induced focusing. To formulate this concept, they successfully achieved the focused patterning of NPs on the surface of thick glass and a polymer substrate (cf. Fig. 9.9) [33]. However, such nonconductive substrates always lead to charge accumulations (from deposited charged NPs and ions) within the nanostructures. The consequence of this was that the incoming charged NPs were repelled and scattered away, resulting in self-termination growth and unwanted deposition of charged NPs onto the mask surface. Therefore, patterning on nonconductive substrates (e.g., thick glass, polymer film) requires means of conducting away the abundant charges. This can be achieved by covering the nonconductive substrate (beneath the mask; cf. Fig. 9.10) with a thin conducting liquid before deposition and evaporate it afterward [33].

Previously, a plastic microstencil mask was already utilized for making a metal pattern with thermal deposition [43]. However, the resolution was limited to tens of microns. Later, Kim et al. proposed a combination of electrospraying with a freestanding mask for patterning thin films of organic or biomacromolecules, with the highest resolution of 2 μm line and space [44]. The weak focusing effect was attributed to the charged particles on the microstencil mask. Similarly, they reported that the aperture patterns of the mask determine the deposited patterns.

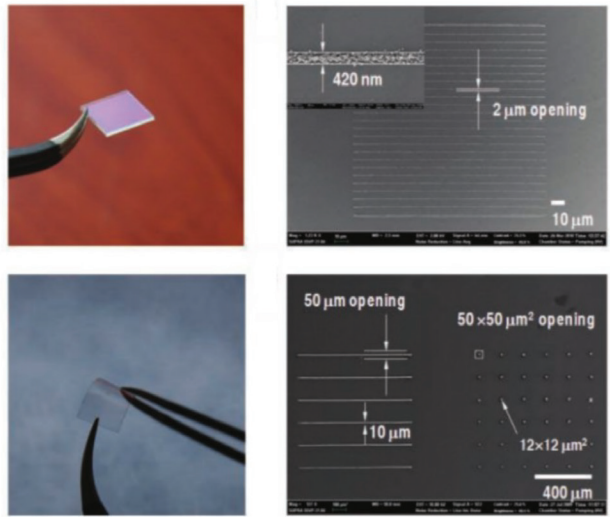

Figure 9.9 Optical and SEM images on the first row are taken from a 0.7-mm-thick glass substrate, while the bottom ones are based on a 0.1-mm-thick polymeric substrate. Reprinted with permission from Ref. [33]. Copyright (2010) Wiley-VCH.

Further enhancing the flexibility of EAAL, Choi's group also used a floating mask or freestanding mask instead of directly placing a mask on a substrate (cf. Fig. 9.10) [45]. Such modification not only simplifies the patterning procedures but also enables the increase of array density and patterning of different material NPs on the same substrate by sequential deposition, synchronized with lateral mask translation [33, 45]. Therefore, the floating mask imparts the most important feature of the noncontact printing technique that may work for complex surfaces of substrates. A detailed study on this by Choi's group is ongoing [46].

In addition, the freestanding mask allows sputtering a metallic film (100 nm thick), where an electric potential difference can be made to a negatively biased substrate (cf. Fig. 9.11). Doing so was proven to also reshape the electric field streamlines [45], similar to the ion-induced electrostatic lens effect. Raising the potential difference was shown to scale down the nanostructure patterns [45].

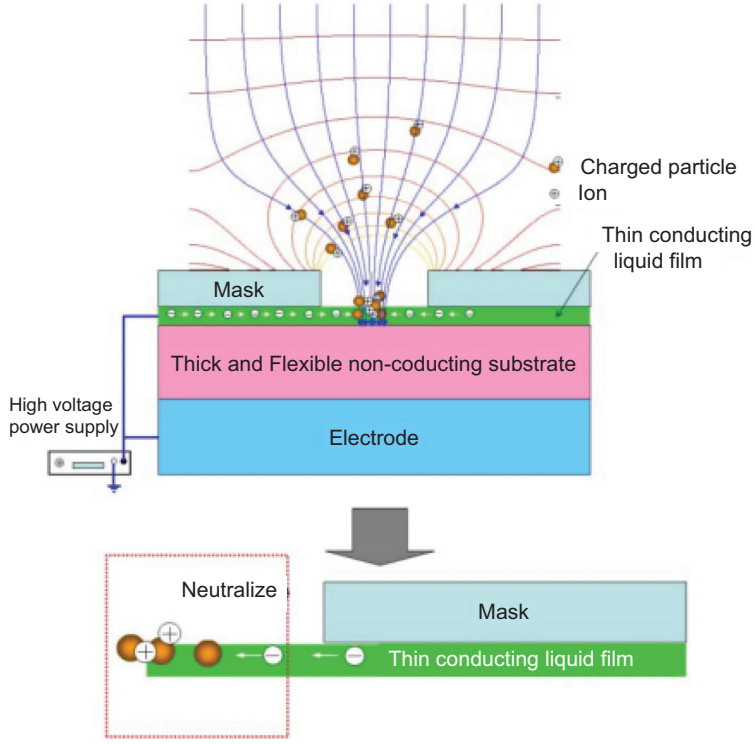

Figure 9.10 Conducting liquid film coating on a nonconductive substrate and charge neutralization beneath the mask. Reprinted with permission from Ref. [33]. Copyright (2010) Wiley-VCH.

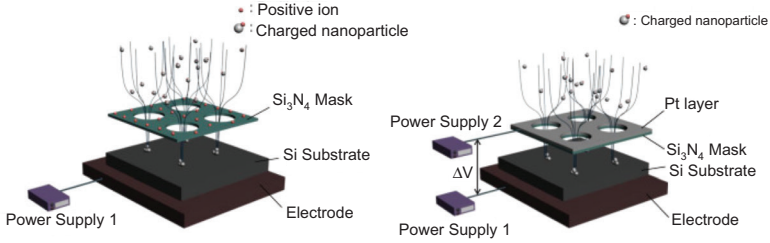

Figure 9.11 Comparison of the focusing effect induced by ion accumulation (left) and by the potential difference between the floating mask and the substrate (right). The stencil mask and the Si substrate were separated by 4 µm using a nanopositioning stage. Reprinted from Ref. [45]. Copyright (2015), with permission from Elsevier.

9.3.4 Parallel Patterning of 3D Nanostructures on a Large Surface Area

To lodge practical applications, the most important goal is to enlarge the patterned surface area with great uniformity. Choi's group already successfully scaled up the patterning of 3D nanostructures on a surface from the order of 100 μm × 100 μm to that of 50,000 μm × 50,000 μm [24]. The core concept was to enlarge the cloud of charged aerosols above the surface of a substrate, circumventing the spatially non-uniform concentration profile from a "point particle source." To address that, they developed multiple pins to holes on a plate electrode (cf. Fig. 9.12a). Using this setup, the nanostructure arrays show a constant height and diameter at a surface area of 50,000 μm × 50,000 μm (cf. Fig. 9.12b,c) [24].

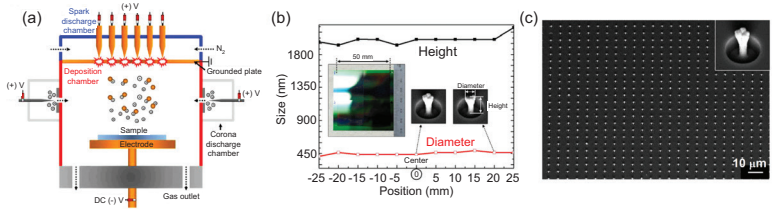

Figure 9.12 Patterning 3D nanostructure arrays by using the spark discharge configuration equipped with multiple pins to holes on a plate electrode in spark ablation (a) and demonstration of the parallelism of the nanostructure arrays (b, c). Reprinted from Ref. [24]. © IOP Publishing. Reproduced with permission. All rights reserved.

9.3.5 Remarks on Spark-Produced NPs for Patterning 3D Nanostructures

The charging probability for spark-produced NPs is roughly about 5% [19], much higher than in most other aerosol generation methods. Simultaneously, the spark plasma also contains gas ions. Making such combined charged species is a unique advantage for focused deposition of charged NPs to form 3D nanostructures. Even more, the NP size generally lies below 10 nm (also having a narrow size distribution) [17], thus only carrying one elementary charge and effectively eliminating inertial impaction [36]. In this regard, the motion of singly charged NPs is strictly dominated by the

external electrical field, and a process for reducing particle charge is not necessary [36]. A third unique feature is that spark-produced NPs can be highly pure, promoting local particle coalescence upon deposition within the NP structures. Such local coalescence helps to compact the nanostructures and thus to improve their conductivity. Finally, the unlimited mixing combinations give great versatility to the materials of 3D nanostructures, broadening future applications.

9.4 Applications

9.4.1 Gas Sensors

Gas molecules diffuse to nanopatterns consisting of NPs, which leads to a change in electrical or optical properties, from which an electrical signal can be derived. This signal is correlated to the concentration of the gas (e.g., CO and H_2). The sensing device based on an NP line pattern was reported to be capable of detecting the CO concentration down to 1 ppm [33]. Its sensitivity, in principle, can further be enhanced by changing the width of the patterned lines, in accordance with the opening space of the patterned mask.

Apart from the line patterns for gas sensors [33], EAAL was also applied to make 3D microstructures that are mutually bridged but floating over a substrate [34, 41]. This enables further advancing interconnects used in sensors [34], nanoelectronics [47], etc. This point is illustrated with an example drawn from previous work [34]. Figure 9.7a shows a dielectric layer having three holes positioned at the vertices and one hole located at the orthocenter of an equilateral triangle (edge length ca. 5.8 μm; hole diameter 1 μm). The charged NPs were initially focused into the center of each opening. The structures grew upward to a comparable thickness of the patterns, terminating their vertical growth while transforming into lateral growth toward the center. The nanostructure at the center hole opens three bridges toward the nanostructures grown from the three holes at the vertices. These nanostructures were eventually connected, as shown in the rightmost panel in Fig. 9.7a. Applying this principle, a CO gas sensor was made based on the tetra-furcated Cu NP structure, and its response was enhanced by a factor of more than 2 for CO at 100 ppm compared to the NP film [34]. The asymmetric

NP structures can be further modified to establish multidirectional networks and junctions suitable for nanoelectronics, sensors, etc.

Depositing different functional NPs either above or below an NP film was reported to considerably improve the conductivity of NP structures, thereby delivering exceptionally high sensitivity in solid-state gas sensors [48]. This concept can be integrated into EAAL for patterning NP structures used in sensing devices or other nanodevices.

9.4.2 Plasmonic Sensors

Plasmonics offers a key to improve the efficiency in widespread applications (see also Chapter 12) [49]. Storing part of their energy in the electron gas of a metal, surface plasmons are capable of creating strongly localized and intense optical fields, which consequently enhance a range of optical processes. Known examples are surface-enhanced Raman scattering (SERS), metal-enhanced fluorescence (MEF), and plasmonic solar cells. MEF has been proven to improve fluorescence intensities of luminescent probes [50], useful in sensitive detection of biomolecules (cf. Chapter 13).

MEF stems from the plasmon resonance of metal NPs (e.g., silver or gold) that interact with a fluorophore. This leads to enhancement of excitation rates through local field amplification and to an increase in emission efficiency by enhanced radiative decay rates, both of which contribute to an overall increase in fluorescent emission intensities (see Chapter 13 for biomedical applications of this effect). The increase of luminescence up-conversion was theoretically predicted to follow a fourth-power dependence on local field enhancement, but the typical gains are weaker than in SERS [51]. According to this theory, human immunoglobulin G–fluorescein isothiocyanate (IgG-FITC; Sigma, F9636) deposited on top of Ag nanostructures was shown to emit a significantly improved fluorescence signal (cf. Fig. 9.13) [37]. The work distinguishes from a traditional dipping process, as it makes a desired locus through stacking different materials layer by layer [37]. In the traditional process, it relies on dipping a metal-prepatterned substrate into a protein solution, followed by washing away the proteins absorbed on the nonmetallic parts. Still, some residual proteins are absorbed, thus producing an unwanted background signal.

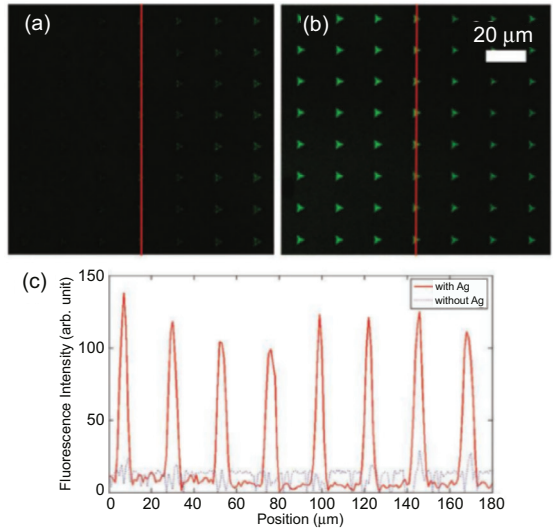

Figure 9.13 Considerably improved fluorescence signal. Confocal microscopic images are corresponding to (a) IgG-FITC and (3) IgG-FITC/Ag nanostructrues. (c) The fluorescence signal is shown to be enhanced by a factor of roughly 6. Reprinted with permission from Ref. [37]. Copyright (2011) Wiley-VCH.

Raman scattering by a single molecule has been reported, with an intensified signal up to the order of 10^{14} [52], due to the hotspot (produced by Ag/Au nanostructures)-induced local field enhancement. One may notice that the enhancement here is much stronger than the case of fluorescence. This is because Raman scattering is a coherent process in contrast to the typically incoherent absorption-emission fluorescence (excited-state absorption and nonradiative energy transfer differ from Raman scattering) [51].

Flower 3D nanostructures were shown to have electromagnetic hotspots at the 3D nanogaps between adjacent petals. Choi's group has shown that electromagnetic hotspots can be engineered by the number of petals (cf. Fig. 9.14a,b) [53]. Figure 9.14c,d shows that an increase in the number of petals leads to an increased number of hotspots, thereby enhancing the field intensity significantly. In comparison with the particle film, such 3D nanostructures were shown to improve the intensity of Raman scattering by around 2 orders of magnitude [53].

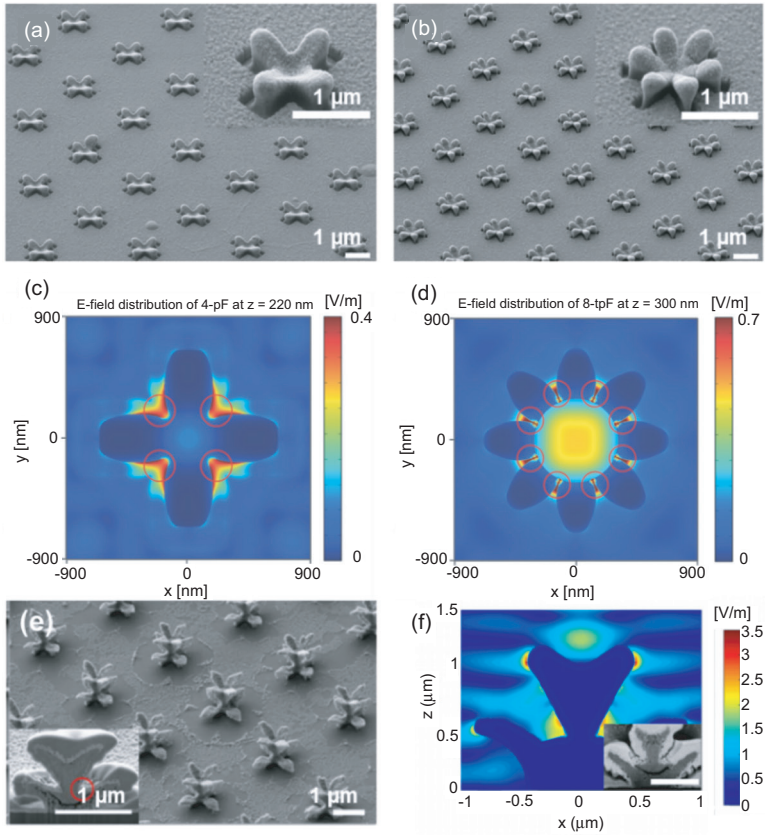

Figure 9.14 (a) SEM image of 3D nanostructures with four petals. (b) SEM image of 3D nanostructures with eight petals. (c) Calculated electric field intensity distribution of 3D nanostructure with four petals at z = 220 nm. (d) Calculated electric field intensity distribution of 3D nanostructure with eight petals at z = 300 nm. Reprinted with permission from Ref. [53]. Copyright (2014) Wiley-VCH. (e) SEM image of stacked bilayer 3D nanostructures. (f) Calculated electric field intensity distribution of vertical cross section. Reprinted from Ref. [35]. © IOP Publishing. Reproduced with permission. All rights reserved.

Furthermore, Lee et al. demonstrated that additional vertical hotspots can be created by vertical-stacking 3D nanostructures through consecutive execution of EAAL and e-beam lithography (Fig. 9.14e) [35]. They discovered that even though the number of hotspots was increased twice, SERS peak intensity was enhanced by more than fivefold. Such disproportional enhancement was

attributed to additional vertical hotspots created near the pillar connecting the upper and lower 3D nanostructures, as shown in Fig. 9.14f.

9.4.3 Solar Cells

Solar cells are another attractive field for exploiting 3D nanostructures, which have optical advantages such as electromagnetic hotspots or cavities. 3D nanostructures made by EAAL were shown to improve the efficiency and performance of solar cells. Ha et al. demonstrated that the power conversion efficiency of nc-Si:H thin-film solar cells can be improved by up to 22% by incorporating 3D nanostructures (Fig. 9.15a) [54]. This enhancement was attributed to the surface plasmon resonances surrounding the structures at multiple frequencies, which increase the light scattering and the absorption

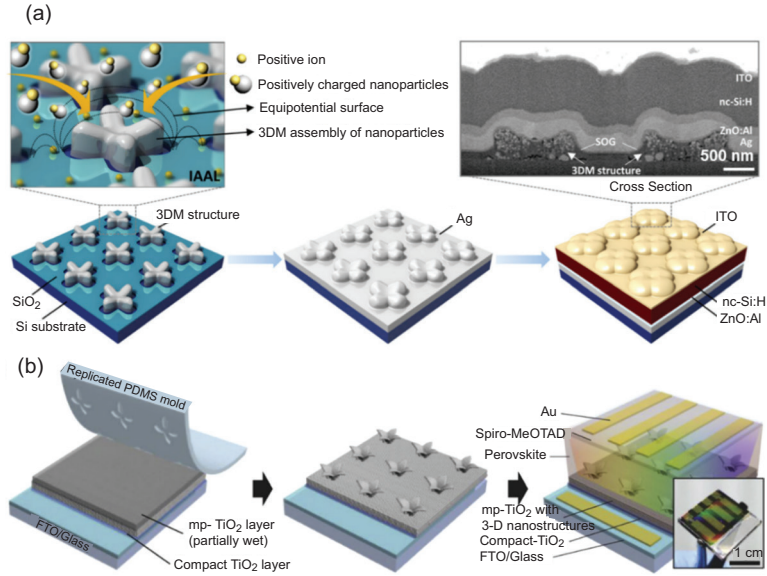

Figure 9.15 (a) Schematic illustration for the preparation of an nc-Si:H thin-film solar cell using 3D nanostructures via ion-assisted aerosol lithography (IAAL). Reprinted from Ref. [54]. © IOP Publishing. Reproduced with permission. All rights reserved. (b) Schematic illustration of patterning of TiO_2 using a PDMS mold and fabrication of a perovskite solar cell incorporating 3D nanostructures. Reprinted from Ref. [55], Copyright (2016), with permission from Elsevier.

efficiency (see also Chapter 12). Moreover, Jang et al. used a new technology combining 3D assembly via EAAL and soft lithography to fabricate 3D-nanopatterned TiO_2 electrodes [55]. As shown in Fig. 9.15b, they made 3D-patterned TiO_2 electrodes by stamping 3D patterned polydimethylsiloxane (PDMS) molds replicated from 3D nanostructures via EAAL. By employing 3D-patterned TiO_2 electrodes, perovskite solar cells can exhibit improved optoelectronic performance and enhanced charge collection due to effective light harvesting. Their work improved the approximate average values of short-circuit current density by 5%, the open-circuit voltage by 2%, the fill factor by 3%, and the photon conversion efficiency by 10%, in reference to those with flat TiO_2.

9.5 Conclusions

We have described the implementation of aerosol technologies for EAAL to print 3D nanostructure arrays, together with some applications. In this method, the transport of charged aerosols is directed to precisely addressable/programmable locations with nanometer resolution on a surface, eventually structuring to arrays of complex 3D nano-/micropatterns. In principle, this process should work with any material that can be converted to charged aerosols. In this respect, spark ablation is a perfect match for EAAL in terms of making uniform/compact 3D nanostructure arrays, even on a macroscale surface. For example, it can be modified to supply sub-10-nm building blocks consistently, and this consistent production was maintained when sparking multiple pairs of electrodes in parallel. Considering all the developments (particularly the concept of a floating mask), EAAL bears great potential for further development to a noncontact 3D nanoprinting technology that enables the manufacturing of 3D nano-/microstructures on a mass/macroscale.

References

1. Su, Y. W., Wu, C. S., Chen, C. C. and Chen, C. D. (2003). Fabrication of two-dimensional arrays of CdSe pillars using E-beam lithography and electrochemical deposition, *Adv. Mater.*, **15**(1), pp. 49–51.

2. Yamazaki, K. and Yamaguchi, H. (2012). Electron beam lithography on vertical side faces of micrometer-order Si block, *J. Vac. Sci. Technol., B*, **30**(4), p. 041601.
3. Feng, J., Tuominen, M. T. and Rothstein, J. P. (2011). Hierarchical superhydrophobic surfaces fabricated by dual-scale electron-beam-lithography with well-ordered secondary nanostructures, *Adv. Funct. Mater.*, **21**(19), pp. 3715–3722.
4. Keskinbora, K., Grevent, C., Hirscher, M., Weigand, M. and Schutz, G. (2015). Single-step 3D nanofabrication of kinoform optics via gray-scale focused ion beam lithography for efficient x-ray focusing, *Adv. Opt. Mater.*, **3**(6), pp. 792–800.
5. Li, Z., Siklos, M., Pucher, N., Cicha, K., Ajami, A., Husinsky, W., Rosspeintner, A., Vauthey, E., Gescheidt, G., Stampfl, J. and Liska, R. (2011). Synthesis and structure-activity relationship of several aromatic ketone-based two-photon initiators, *J. Polym. Sci., Part A: Polym. Chem.*, **49**(17), pp. 3688–3699.
6. Ovsianikov, A., Viertl, J., Chichkov, B., Oubaha, M., MacCraith, B., Sakellari, I., Giakoumaki, A., Gray, D., Vamvakaki, M., Farsari, M. and Fotakis, C. (2008). Ultra-low shrinkage hybrid photosensitive material for two-photon polymerization microfabrication, *ACS Nano*, **2**(11), pp. 2257–2262.
7. Wilbur, J. L., Kumar, A., Biebuyck, H. A., Kim, E. and Whitesides, G. M. (1996). Microcontact printing of self-assembled monolayers: applications in microfabrication, *Nanotechnology*, **7**(4), pp. 452–457.
8. Cui, Y., Björk, M. T., Liddle, J. A., Sönnichsen, C., Boussert, B. and Alivisatos, A. P. (2004). Integration of colloidal nanocrystals into lithographically patterned devices, *Nano Lett.*, **4**(6), pp. 1093–1098.
9. Kraus, T., Malaquin, L., Schmid, H., Riess, W., Spencer, N. D. and Wolf, H. (2007). Nanoparticle printing with single-particle resolution, *Nat. Nanotechnol.*, **2**(9), pp. 570–576.
10. Park, J. U., Hardy, M., Kang, S. J., Barton, K., Adair, K., Mukhopadhyay, D. K., Lee, C. Y., Strano, M. S., Alleyne, A. G., Georgiadis, J. G., Ferreira, P. M. and Rogers, J. A. (2007). High-resolution electrohydrodynamic jet printing, *Nat. Mater.*, **6**(10), pp. 782–789.
11. Galliker, P., Schneider, J., Eghlidi, H., Kress, S., Sandoghdar, V. and Poulikakos, D. (2012). Direct printing of nanostructures by electrostatic autofocussing of ink nanodroplets, *Nat. Commun.*, **3**, p. 890.
12. Tarafder, S., Balla, V. K., Davies, N. M., Bandyopadhyay, A. and Bose, S. (2013). Microwave-sintered 3D printed tricalcium phosphate scaffolds

for bone tissue engineering, *J. Tissue Eng. Regen. Med.*, **7**(8), pp. 631–641.

13. Khalyfa, A., Vogt, S., Weisser, J., Grimm, G., Rechtenbach, A., Meyer, W. and Schnabelrauch, M. (2007). Development of a new calcium phosphate powder-binder system for the 3D printing of patient specific implants, *J. Mater. Sci. Mater. Med.*, **18**(5), pp. 909–916.
14. Schwyn, S., Garwin, E. and Schmidt-Ott, A. (1988). Aerosol generation by spark discharge, *J. Aerosol Sci.*, **19**(5), pp. 639–642.
15. Tabrizi, N. S., Ullmann, M., Vons, V. A., Lafont, U. and Schmidt-Ott, A. (2009). Generation of nanoparticles by spark discharge, *J. Nanopart. Res.*, **11**, pp. 315–332.
16. Pfeiffer, T. V., Feng, J. and Schmidt-Ott, A. (2014). New developments in spark production of nanoparticles, *Adv. Powder Technol.*, **25**(1), pp. 56–70.
17. Feng, J., Guo, X., Ramlawi, N., Pfeiffer, T. V., Geutjens, R., Basak, S., Nirschl, H., Biskos, G., Zandbergen, H. W. and Schmidt-ott, A. (2016). Green manufacturing of metallic nanoparticles: a facile and universal approach to scaling up, *J. Mater. Chem. A*, **4**, pp. 11222–11227.
18. Feng, J. (2016). Scalable spark ablation synthesis of nanoparticles: fundamental considerations and application in textile nanofinishing, TU Delft.
19. Feng, J., Biskos, G. and Schmidt-Ott, A. (2015). Toward industrial scale synthesis of ultrapure singlet nanoparticles with controllable sizes in a continuous gas-phase process, *Sci. Rep.*, **5**, p. 15788.
20. Feng, J., Huang, L., Ludvigsson, L., Messing, M. E., Maisser, A., Biskos, G. and Schmidt-Ott, A. (2016). General approach to the evolution of singlet nanoparticles from a rapidly quenched point source, *J. Phys. Chem. C*, **120**(1), pp. 621–630.
21. Chae, S., Lee, D., Kim, M.-C., Kim, D. S. and Choi, M. (2015). Wire-in-hole-type spark discharge generator for long-time consistent generation of unagglomerated nanoparticles, *Aerosol Sci. Technol.*, **49**(7), pp. 463–471.
22. Han, K., Kim, W., Yu, J., Lee, J., Lee, H., Gyu Woo, C. and Choi, M. (2012). A study of pin-to-plate type spark discharge generator for producing unagglomerated nanoaerosols, *J. Aerosol Sci.*, **52**, pp. 80–88.
23. Noh, S. R., Lee, D., Park, S. J., Kim, D. S. and Choi, M. (2017). High throughput nanoparticle generation utilizing high-frequency spark discharges via rapid spark plasma removal, *Aerosol Sci. Technol.*, **51**(1), pp. 116–122.

24. Ha, K., Choi, H., Jung, K., Han, K., Lee, J.-K., Ahn, K. and Choi, M. (2014). Large-area assembly of three-dimensional nanoparticle structures via ion assisted aerosol lithography with a multi-pin spark discharge generator, *Nanotechnology*, **25**(22), p. 225302.

25. Noh, S. R., Kim, D. S., Park, S. J. and Choi, M. (2016). Enhanced yield of positively charged particles from a spark discharge generator via in situ corona discharges, *J. Aerosol Sci*., **101**, pp. 188–195.

26. Kim, H., Kim, J., Yang, H., Suh, J., Kim, T., Han, B., Kim, S., Kim, D. S., Pikhitsa, P. V. and Choi, M. (2006). Parallel patterning of nanoparticles via electrodynamic focusing of charged aerosols, *Nat. Nanotechnol*., **1**(2), pp. 117–121.

27. Alonso, M., Hernandez-Sierra, A. and Alguacil, F. J. (2003). Electrical charging of aerosol nanoparticles and some practical applications, *Rev. Metal*., **39**, pp. 41–57.

28. Lee, D., Lee, K., Kim, D. S., Lee, J.-K., Park, S. J. and Choi, M. (2017). Hydrogen-assisted spark discharge generation of highly crystalline and surface-passivated silicon nanoparticles, *J. Aerosol Sci*., **114**, pp. 139–145.

29. Feng, J., Geutjens, R., Thang, N. V., Li, J., Guo, X., Kéri, A., Basak, S., Galbács, G., Biskos, G., Nirschl, H., Zandbergen, H. W; Brück, E. and Schmidt-Ott, A. (2018). Magnetic phase transition in spark-produced ternary LaFeSi nanoalloys, *ACS Appl. Mater. Interfaces*, **10**(7), pp. 6073–6078.

30. Ha, K., Choi, H., Jung, K., Han, K., Lee, J. K., Ahn, K. and Choi, M. (2014). Large-area assembly of three-dimensional nanoparticle structures via ion assisted aerosol lithography with a multi-pin spark discharge generator, *Nanotechnology*, **25**(22), p. 225302.

31. Krinke, T. J., Deppert, K., Magnusson, M. H. and Fissan, H. (2002). Nanostructured deposition of nanoparticles from the gas phase, *Part. Part. Syst. Char*., **19**(5), pp. 321–326.

32. You, S. and Choi, M. (2007). Numerical simulation of microscopic motion and deposition of nanoparticles via electrodynamic focusing, *Aerosol Sci*., **38**, pp. 1140–1149.

33. You, S., Han, K., Kim, H., Lee, H., Woo, C. G., Jeong, C., Nam, W. and Choi, M. (2010). High-resolution, parallel patterning of nanoparticles via an ion-induced focusing mask, *Small*, **6**(19), pp. 2146–2152.

34. Bae, Y., Pikhitsa, P. V., Cho, H. and Choi, M. (2017). Multifurcation assembly of charged aerosols and its application to 3D structured gas sensors, *Adv. Mater*., **29**(2), p.1604159.

35. Lee, K., Choi, H., Kim, D. S., Jang, M. S. and Choi, M. (2017). Vertical stacking of three-dimensional nanostructures via an aerosol lithography for advanced optical applications, *Nanotechnology*, **28**(47), p. 475302.

36. Lee, H., You, S., Woo, C. G., Lim, K., Jun, K. and Choi, M. (2009). Focused patterning of nanoparticles by controlling electric field induced particle motion, *Appl. Phys. Lett.*, **94**(5), p. 053104.

37. Woo, C. G., Shin, H., Jeong, C., Jun, K., Lee, J., Lee, J.-R., Lee, H., You, S., Son, Y. and Choi, M. (2011). Selective nanopatterning of protein via ion-induced focusing and its application to metal-enhanced fluorescence, *Small*, **7**(13), pp. 1790–1794.

38. Xie, J., Rezvanpour, A., Wang, C.-H. and Hua, J. (2010). Electric field controlled electrospray deposition for precise particle pattern and cell pattern formation, *AIChE J.*, **56**(10), pp. 2607–2621.

39. Suh, J., Han, B., Okuyama, K. and Choi, M. (2005). Highly charging of nanoparticles through electrospray of nanoparticle suspension, *J. Colloid Interface Sci.*, **287**(1), pp. 135–140.

40. Hoppel, W. A. and Frick, G. M. (1986). Ion—aerosol attachment coefficients and the steady-state charge distribution on aerosols in a bipolar ion environment, *Aerosol Sci. Technol.*, **5**(1), pp. 1–21.

41. Lee, H., You, S., Pikhitsa, P. V; Kim, J., Kwon, S., Woo, C. G. and Choi, M. (2011). Three-dimensional assembly of nanoparticles from charged aerosols, *Nano Lett.*, **11**(1), pp. 119–124.

42. Choi, M., Lee, H., You, S. and Woo, C. (2008). Array formation of 3-D nanostructure of nanoparticle via electrodynamic focusing of charged aerosols, *AAAR 27th Annual Conference*, Florida, p. 55.

43. Kim, G., Kim, B. and Brugger, J. (2003). All-photoplastic microstencil with self-alignment for multiple layer shadow-mask patterning, *Sens. Actuators, A*, **107**(2), pp. 132–136.

44. Kim, J. W., Yamagata, Y., Kim, B. J. and Higuchi, T. (2009). Direct and dry micro-patterning of nano-particles by electrospray deposition through a micro-stencil mask, *J. Micromech. Microeng.*, **19**(2), p. 025021.

45. Choi, H., Kang, S., Jung, W., Jung, Y. ho; Park, S. J., Kim, D. S. and Choi, M. (2015). Controlled electrostatic focusing of charged aerosol nanoparticles via an electrified mask, *J. Aerosol Sci.*, **88**, pp. 90–97.

46. Choi, M. (2018). Three dimensional nanoprinting via aerosol technology, *Aerosol Technology*, Bilbao.

47. Atabaki, A. H., Moazeni, S., Pavanello, F., Gevorgyan, H., Notaros, J., Alloatti, L., Wade, M. T., Sun, C., Kruger, S. A., Meng, H., Qubaisi, K. A.,

Wang, I; Zhang, B., Khilo, A., Baiocco, C. V., Popović, M. A., Stojanović, V. M. and Ram, R. J. (2018). Integrating photonics with silicon nanoelectronics for the next generation of systems on a chip, *Nature*, **556**(7701), pp. 349–354.

48. Tricoli, A. and Pratsinis, S. E. (2010). Dispersed nanoelectrode devices, *Nat*. *Nanotechnol*., **5**(1), pp. 54–60.
49. Aslam, U., Chavez, S. and Linic, S. (2017). Controlling energy flow in multimetallic nanostructures for plasmonic catalysis, *Nat*. *Nanotechnol*., **12**(10), pp. 1000–1005.
50. Yin, D., Wang, C., Ouyang, J., Zhang, X., Jiao, Z., Feng, Y., Song, K., Liu, B., Cao, X., Zhang, L., Han, Y. and Wu, M. (2014). Synthesis of a novel core–shell nanocomposite Ag@SiO_2 @Lu_2O_3:Gd/Yb/Er for large enhancing upconversion luminescence and bioimaging, *ACS Appl*. *Mater*. *Interfaces*, **6**(21), pp. 18480–18488.
51. Esteban, R., Laroche, M. and Greffet, J. J. (2009). Influence of metallic nanoparticles on upconversion processes, *J*. *Appl*. *Phys*., **105**(3), p. 033107.
52. Lu, D., Cho, S. K., Ahn, S., Brun, L., Summers, C. J. and Park, W. (2014). Plasmon enhancement mechanism for the upconversion processes in $NaYF_4$:Yb^{3+},Er^{3+} nanoparticles: Maxwell *versus* Förster, *ACS Nano*, **8**(8), pp. 7780–7792.
53. Jung, K., Hahn, J., In, S., Bae, Y., Lee, H., Pikhitsa, P. V., Ahn, K., Ha, K., Lee, J.-K., Park, N. and Choi, M. (2014). Hotspot-engineered 3D multipetal flower assemblies for surface-enhanced Raman spectroscopy, *Adv*. *Mater*., **26**(34), pp. 5924–5929.
54. Ha, K., Jang, E., Jang, S., Lee, J. K., Jang, M. S., Choi, H., Cho, J. S. and Choi, M. (2016). A light-trapping strategy for nanocrystalline silicon thin-film solar cells using three-dimensionally assembled nanoparticle structures, *Nanotechnology*, ***27***(5), p. 055403.
55. Jang, S., Yoon, J., Ha, K., Kim, M., Kim, D. H., Kim, S. M., Kang, S. M., Park, S. J., Jung, H. S. and Choi, M. (2016). Facile fabrication of three-dimensional TiO_2 structures for highly efficient perovskite solar cells, *Nano Energy*, **22**, pp. 499–506.